

Article

Effects of Pre-Stretching Amount on Motion Characteristics and Screening Efficiency of Flip-Flow Screen Plates

Yixin Wang, Runhui Geng , Wanqing Yu, Dongdong Lin, Ziqian Wang and Xinwen Wang *

School of Chemical and Environmental Engineering, China University of Mining and Technology (Beijing), Beijing 100083, China; bqt2100301003t@student.cumtb.edu.cn (Y.W.)

* Correspondence: xinwen.w@cumtb.edu.cn

Abstract: This study systematically investigates the impact of pre-stretching amount (PSA) on the acceleration, motion status, and screening efficiency of the Flip-flow screen plate (FFSP). Initially, a nonlinear spring-multi-body model of the FFSP is established. Subsequently, the acceleration signals at the midpoint of the FFSP under various PSAs are measured and analyzed. The nonlinear stiffness coefficient of FFSP along the vertical direction is then determined and it is found that simplifying the nonlinear spring-multi-body system to a nonlinear spring-tri-body system under the experimental conditions can maintain the calculation error of FFSP's acceleration within 30%. Phase and Poincaré mapping diagrams of the FFSP under different PSAs are subsequently created to illustrate the impact of PSA on the motion status of the FFSP. Finally, screening experiments are performed to study the optimal PSA for a kind of bituminous coal from Shanxi province.

Keywords: pre-stretching amount; flip-flow screen; motion characteristics; screening efficiency



Citation: Wang, Y.; Geng, R.; Yu, W.; Lin, D.; Wang, Z.; Wang, X. Effects of Pre-Stretching Amount on Motion Characteristics and Screening Efficiency of Flip-Flow Screen Plates. *Minerals* **2024**, *14*, 472. <https://doi.org/10.3390/min14050472>

Academic Editor: Luis Marcelo Tavares

Received: 25 March 2024

Revised: 18 April 2024

Accepted: 26 April 2024

Published: 29 April 2024



Copyright: © 2024 by the authors. Licensee MDPI, Basel, Switzerland. This article is an open access article distributed under the terms and conditions of the Creative Commons Attribution (CC BY) license (<https://creativecommons.org/licenses/by/4.0/>).

1. Introduction

Coal is a kind of significant fossil energy, accounting for about 40% [1–3] of the global fuel used to generate electricity. However, harmful gases are emitted during the process of burning coal, so raw coal needs to be processed before industrial application in order to improve the cleanliness of coal and reduce environmental pollution caused by sulfur dioxide and nitrogen oxides, etc. Currently, mineral processing is considered as an economical and effective way to improve the cleanliness of raw coal [4–9]. Screening is an important component of mineral processing [10]. According to statistics, screening equipment accounts for 25–33% [11] of the total number of equipment in modern coal processing plants. Therefore, research on screening equipment is of great significance to industrial production [12–16].

Various screening equipment, such as circular vibrating screens, linear vibrating screens, and arc screens, are widely utilized in coal processing plants for the classification of particles in industrial production. These equipment have demonstrated commendable effectiveness [17].

However, challenges arise during the screening process due to the tendency of moist fine particles to agglomerate or adhere to the screens [18]. This adhesion leads to the phenomenon of hole blocking and reduced efficiency of traditional vibrating screens. Therefore, flip-flow screens with flexible screen plates have been designed to overcome these limitations and enable effective screening of moist fine particles.

Due to the self-cleaning efficacy facilitated by the repetitive motion of relaxation stretching relaxation of FFSPs, flip-flow screens have gained extensive adoption in the screening process of moist fine materials. This motion pattern generates high acceleration on the surface of the screen plates, effectively addressing the prevalent challenge of hole blocking commonly encountered in industrial screening operations [19–23].

Based on the research conducted by Cao [24], it is observed that the utilization of flip-flow screens in the coal desliming process of the washing system resulted in a significant

reduction in the quantity of coal slime. Consequently, it can be concluded that flip-flow screen is a type of screening equipment with extensive prospects for application, effectively resolving the issue of dry deep screening for moist fines [19,25].

The study of screening efficiency in flip-flow screens has always been a topic of great importance. Researchers have consistently focused on optimizing the screening efficiency by making adjustments to the length of the flip-flow screen or working parameters [26–33]. However, when there are variations in the properties of the feeding, optimizing the screening efficiency through these methods may have certain limitations in industrial production.

For instance, if the length of the flip-flow screen needs to be changed for optimizing the screening efficiency, it requires remanufacturing of the equipment. Similarly, when adjusting the operating parameters to regulate the screening efficiency, the amplitude and frequency of the flip-flow screen are typically adjustable within a limited range to prevent mechanical failures and ensure smooth operation of the screen frame. These constraints can impede the optimization of screening efficiency in industrial production [34,35].

Therefore, there is a need for alternative approaches that can overcome these limitations and achieve optimum screening efficiency even with changes in the feeding's properties.

By adjusting the PSA of the screen plate, the acceleration of the screen plate can be changed across a wide range, providing a convenient way to optimize screening efficiency [36–38]. This method can be achieved without modifying the main body of the flip-flow screen and does not limited by the stability of the screen frames.

The motion process of a FFS with Crank Link Structure is illustrated in Figure 1. The components of the FFS with Crank Link Structure are: the fixed beam, FFSP, moving beam, and the Crank Link Structure.

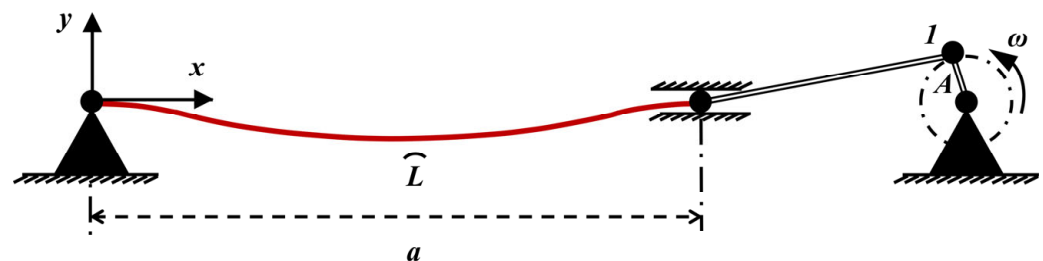


Figure 1. Calculation of PSA of the FFS with Crank Link Structure.

The screen plate, which has an arc length of L , is suspended to two beams on both sides, with a distance of a between them. The two beams have a relative amplitude of size A between them.

Under external excitation, the crank with an eccentricity of A rotates at an angular velocity of ω driving the moving beam to produce reciprocating motion along the x -direction. Within one motion cycle, when the end point 1 of the crank rotates to the far left, the beam spacing between the fixed beam and the moving beam reaches its minimum value a_{min} , and the FFSP is in its most relaxed state for that cycle. As the end point 1 gradually rotates counterclockwise from the far left, the FFSP gradually tightens, and when point 1 reaches the far right position, the beam spacing between the fixed beam and the moving beam reaches its maximum value a_{max} , and the screen plate is in its most tightened state for one motion cycle. Over time, the spacing between the two beam ends changes by an amount of $2A$.

Equation (1) is used to calculate the amount of PSA for the screen plate. When $\Delta l = 0$, the FFSP remains tightened throughout the motion process. As Δl decreases, the FFSP exhibits alternating tightening and relaxed motion states within one motion cycle. Subsequently, when $\Delta l = -2A$, the FFSP remains completely relaxed throughout.

$$\Delta l = a_{min} - L \quad (1)$$

In order to study the impact of PSA on the motion of FFSP, it is essential to establish a mechanical model of the screen plates that can help us to study their motion mechanism.

The following models are included in current research on modeling FFSPs: Zou and Liu [39] proposed a three-segment arc model to describe the geometric properties of FFSPs in a static state; Zhao [40] utilized an elastic press rod model to develop a mechanical model for the FFSP; Xiong [41] proposed an expression for the acceleration at the midpoint of the FFSP by considering the FFSP as a hanging catenary curve suspended between two beams; Chen [20] introduced a string model to describe the motion of FFSPs.

Overall, there is room for improvement in both experimental research on the motion of the screen plate and theoretical model studies. In terms of experimental research, Wang [38,42] et al.'s study indicated that the PSA affects screening efficiency however the changes in PSA leading to alterations in the motion response and motion status of the screen plate were not discussed. As for theoretical research, scholars have made groundbreaking contributions to the construction of the FFSP model yet there is a lack of research on the nonlinear mechanical model of the FFSP. Therefore, in this study, we comprehensively discuss the impact of the PSA on the acceleration signals, motion status, and screening efficiency of the screen plate, and concluded that the nonlinear spring-tri-body model can calculate the acceleration response under the experimental conditions within the calculation error of 30%.

This paper first proposes a nonlinear mechanics model of the FFSP based on its nonlinear characteristics, and obtains the conclusion that the motion response at the midpoint of the screen plate is a nonlinear superposition of the motion responses of the remaining mass blocks, contributing to a deeper theoretical understanding of the FFSP. Secondly, through experiments, the acceleration signals at the midpoint of the FFSP under different PSAs are obtained, and a thorough analysis is conducted, aiding in a comprehensive understanding of the impact of PSA on the change of the FFSP's acceleration. Subsequently, by combining the nonlinear mechanics model of the screen plate with the experimentally obtained acceleration signals, the nonlinear stiffness coefficient of the screen plate in the vertical direction is derived, and the conclusion is drawn that simplifying the nonlinear spring-multi-body model to a non-linear spring-tri-body model under the experimental conditions can control the calculation error within 30%. Additionally, phase and Poincaré mapping diagrams of the midpoint of the FFSP under different PSAs are created to explore the influence of PSA on the motion status of the screen plate. Lastly, screening experiments are conducted to determine the optimal PSA for the bituminous coal from the Shanxi, China.

2. Nonlinear Mechanical Model of FFSP

In this chapter, we propose a nonlinear mechanical model for the FFSP, taking into account its nonlinear characteristics [43,44]. Firstly, we consider the FFSP as a n -degree-of-freedom system. Next, we employ D'Alembert principle to solve the motion of the mass block at any position of the FFSP.

Figure 2 depicts the nonlinear mechanical model of the FFSP, with point O serving as the coordinate origin. This model represents the FFSP as a n -degree-of-freedom system, where n mass blocks are connected in series. The i th mass block has a mass of m_i and is linked with the $(i - 1)$ th and $(i + 1)$ th mass blocks by a nonlinear spring and a damper. The motion of the first mass block corresponds to the floating screen frame, while the motion of the n th mass block corresponds to the fixed screen frame.

Figure 3 shows the force analysis of the i th mass block as it moves.

According to Figure 3, the mass of the $(i - 1)$ th, i th, and $(i + 1)$ th blocks are denoted as m_{i-1} , m_i , and m_{i+1} , respectively. These blocks are connected by a nonlinear spring and a damper.

The force exerted by the nonlinear spring between the $(i - 1)$ th and i th blocks is represented as $f_{k,i-1}$, while the damping force between these two blocks is denoted as $f_{c,i-1}$. Similarly, the force exerted by the nonlinear spring between the i th and $(i + 1)$ th blocks is represented as $f_{k,i}$, while the damping force between these two blocks is denoted as $f_{c,i}$.

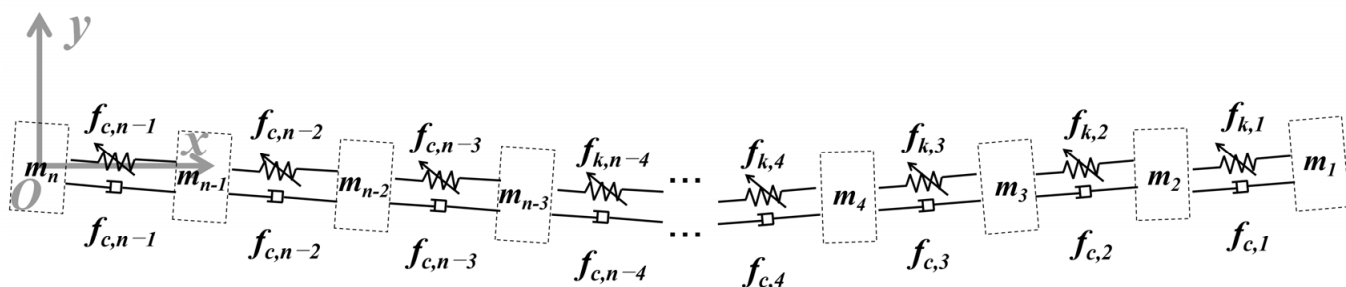


Figure 2. Nonlinear mechanical model for FFSP.

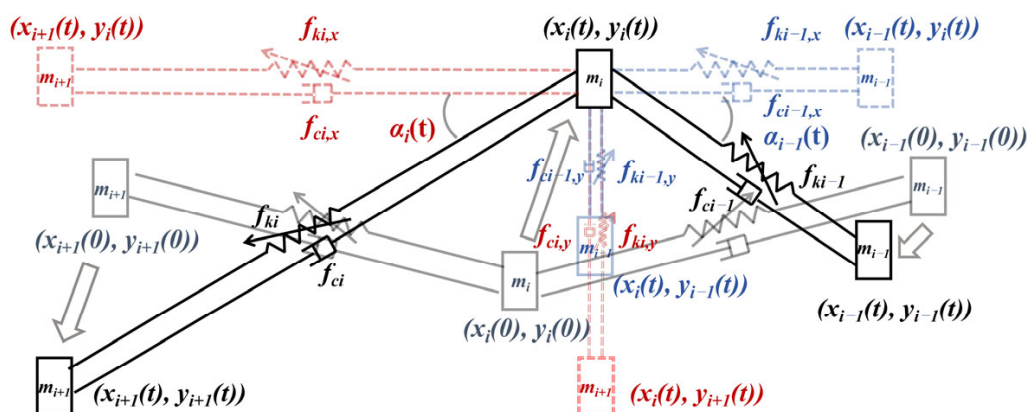


Figure 3. Force analysis of the *i*th mass block during its motion.

The positions of the (*i* − 1)th, *i*th, and (*i* + 1)th mass blocks can be represented by co-ordinates. In the stationary state of the screen plate, these blocks are located at $(x_{i-1}(0), y_{i-1}(0))$, $(x_i(0), y_i(0))$, and $(x_{i+1}(0), y_{i+1}(0))$. At time *t*, their positions shift to $(x_{i-1}(t), y_{i-1}(t))$, $(x_i(t), y_i(t))$, and $(x_{i+1}(t), y_{i+1}(t))$.

At time *t*, the nonlinear elastic forces and damping forces that connect the three mass blocks are decomposed into the *x* and *y* directions. The angle between the total elastic force of the *i*th spring at moment *t* and the elastic force decomposed into the *x*-direction is referred to as $\alpha_i(t)$.

Because the motion of the *i*th mass block is affected by the (*i* − 1)th and (*i* + 1)th mass blocks, we apply D’Alembert principle to list the mechanical expressions for the *i*th mass block in the *x*-direction and *y*-direction. Figures 4 and 5 respectively illustrate the force analysis of the *i*th mass block in the *x* and *y* directions at time *t*.

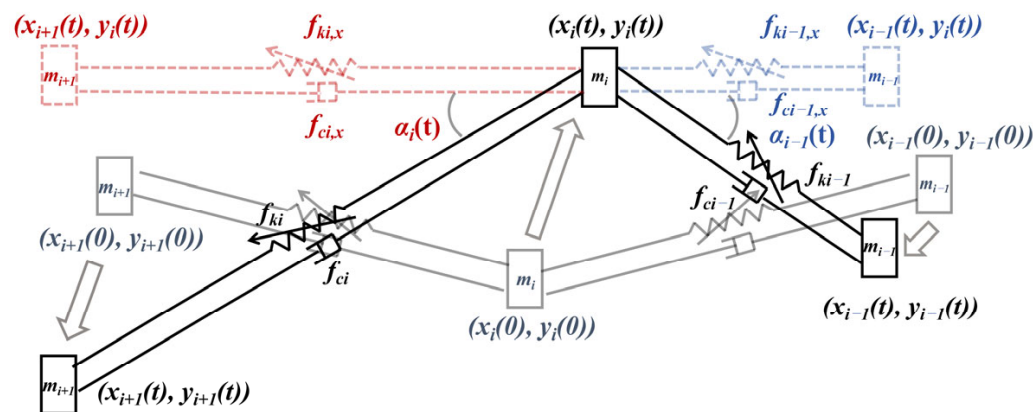


Figure 4. *x*-direction force analysis of *i*th mass block at time *t*.

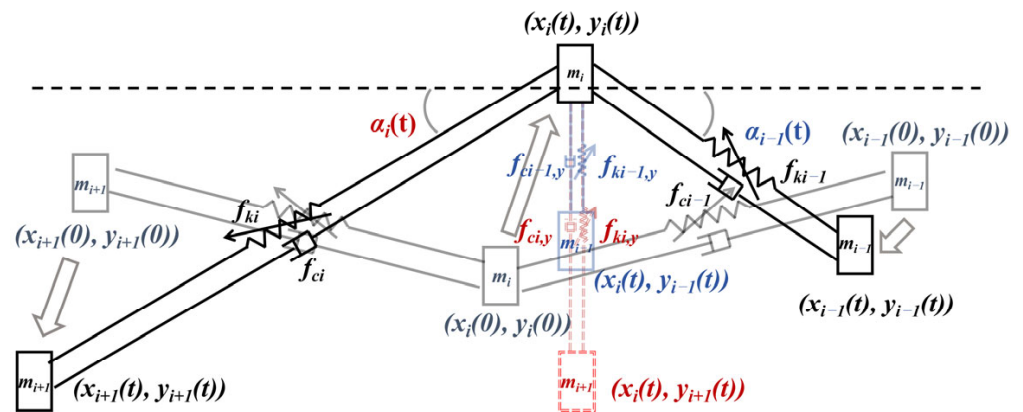


Figure 5. y -direction force analysis of i th mass block at time t .

At moment t , the mechanical expression for the i th mass block in the x -direction is:

$$m_i \ddot{x}_i(t) + [f_{k,i-1}(t) + f_{c,i-1}(t)]\cos\alpha_{i-1}(t) + [f_{k,i}(t) + f_{c,i}(t)]\cos\alpha_i(t) = 0 \quad (2)$$

Among Equation (2)

$$\cos\alpha_{i-1}(t) = \frac{x_{i-1}(t) - x_i(t)}{\sqrt{[x_i(t) - x_{i-1}(t)]^2 + [y_i(t) - y_{i-1}(t)]^2}} \quad (3)$$

At moment t , the mechanical expression for the i th mass block in the y -direction is:

$$m_i \ddot{y}_i(t) + [f_{k,i-1}(t) + f_{c,i-1}(t)]\sin\alpha_{i-1}(t) + [f_{k,i}(t) + f_{c,i}(t)]\sin\alpha_i(t) = 0 \quad (4)$$

Among Equation (4)

$$\sin\alpha_i(t) = \frac{y_i(t) - y_{i-1}(t)}{\sqrt{[x_i(t) - x_{i-1}(t)]^2 + [y_i(t) - y_{i-1}(t)]^2}} \quad (5)$$

The nonlinear elastic force of the i th nonlinear spring can be expressed using a polynomial form:

$$f_{k,i}(t) = b_{i,0} + b_{i,1}[\sqrt{[x_{i+1}(t) - x_i(t)]^2 + [y_{i+1}(t) - y_i(t)]^2} - \sqrt{[x_{i+1}(0) - x_i(0)]^2 + [y_{i+1}(0) - y_i(0)]^2}]^2 + b_{i,2}[\sqrt{[x_{i+1}(t) - x_i(t)]^2 + [y_{i+1}(t) - y_i(t)]^2} - \sqrt{[x_{i+1}(0) - x_i(0)]^2 + [y_{i+1}(0) - y_i(0)]^2}]^3 + \dots + b_{i,q}[\sqrt{[x_{i+1}(t) - x_i(t)]^2 + [y_{i+1}(t) - y_i(t)]^2} - \sqrt{[x_{i+1}(0) - x_i(0)]^2 + [y_{i+1}(0) - y_i(0)]^2}]^q \quad (6)$$

By analyzing the forces acting on the 2nd, 3rd, 4th, ..., and $(n - 1)$ th mass blocks separately in the x -direction and y -direction at time t , we can obtain the following:

$$\begin{pmatrix} m_2 \\ m_3 \\ \dots \\ m_{n-2} \\ m_{n-1} \end{pmatrix} \begin{pmatrix} \ddot{x}_2(t) \\ \ddot{x}_3(t) \\ \dots \\ \ddot{x}_{n-2}(t) \\ \ddot{x}_{n-1}(t) \end{pmatrix} + \begin{pmatrix} \cos\alpha_1(t) \\ \cos\alpha_2(t) \\ \dots \\ \cos\alpha_{n-2}(t) \end{pmatrix} \begin{pmatrix} f_{k,1}(t) \\ f_{k,2}(t) \\ \dots \\ f_{k,n-3}(t) \\ f_{k,n-2}(t) \end{pmatrix} + \begin{pmatrix} c_1 \\ c_2 \\ \dots \\ c_{n-2} \end{pmatrix} \begin{pmatrix} \dot{x}_2(t) - \dot{x}_1(t) \\ \dot{x}_3(t) - \dot{x}_2(t) \\ \dots \\ \dot{x}_{n-2}(t) - \dot{x}_{n-3}(t) \\ \dot{x}_{n-1}(t) - \dot{x}_{n-2}(t) \end{pmatrix} + \begin{pmatrix} \cos\alpha_2(t) \\ \cos\alpha_3(t) \\ \dots \\ \cos\alpha_{n-2}(t) \\ \cos\alpha_{n-1}(t) \end{pmatrix} \begin{pmatrix} f_{k,2}(t) \\ f_{k,3}(t) \\ \dots \\ f_{k,n-2}(t) \\ f_{k,n-1}(t) \end{pmatrix} + \begin{pmatrix} c_2 \\ c_3 \\ \dots \\ c_{n-2} \\ c_{n-1} \end{pmatrix} \begin{pmatrix} \dot{x}_2(t) - \dot{x}_3(t) \\ \dot{x}_3(t) - \dot{x}_4(t) \\ \dots \\ \dot{x}_{n-2}(t) - \dot{x}_{n-1}(t) \\ \dot{x}_{n-1}(t) - \dot{x}_n(t) \end{pmatrix} = \begin{pmatrix} 0 \\ 0 \\ \dots \\ 0 \end{pmatrix} \quad (7)$$

$$\begin{pmatrix} m_2 \\ m_3 \\ \dots \\ m_{n-2} \\ m_{n-1} \end{pmatrix} \begin{pmatrix} \ddot{y}_2(t) \\ \ddot{y}_3(t) \\ \dots \\ \ddot{y}_{n-2}(t) \\ \ddot{y}_{n-1}(t) \end{pmatrix} + \begin{pmatrix} \sin\alpha_1(t) \\ \sin\alpha_2(t) \\ \dots \\ \sin\alpha_{n-3}(t) \\ \sin\alpha_{n-2}(t) \end{pmatrix} \begin{pmatrix} f_{k,1}(t) \\ f_{k,2}(t) \\ \dots \\ f_{k,n-3}(t) \\ f_{k,n-2}(t) \end{pmatrix} + \begin{pmatrix} c_1 \\ c_2 \\ \dots \\ c_{n-3} \\ c_{n-2} \end{pmatrix} \begin{pmatrix} \dot{y}_2(t) - \dot{y}_1(t) \\ \dot{y}_3(t) - \dot{y}_2(t) \\ \dots \\ \dot{y}_{n-2}(t) - \dot{y}_{n-3}(t) \\ \dot{y}_{n-1}(t) - \dot{y}_{n-2}(t) \end{pmatrix} + \begin{pmatrix} \cos\alpha_2(t) \\ \cos\alpha_3(t) \\ \dots \\ \cos\alpha_{n-2}(t) \\ \cos\alpha_{n-1}(t) \end{pmatrix} \begin{pmatrix} f_{k,2}(t) \\ f_{k,3}(t) \\ \dots \\ f_{k,n-2}(t) \\ f_{k,n-1}(t) \end{pmatrix} + \begin{pmatrix} c_2 \\ c_3 \\ \dots \\ c_{n-2} \\ c_{n-1} \end{pmatrix} \begin{pmatrix} \dot{y}_2(t) - \dot{y}_3(t) \\ \dot{y}_3(t) - \dot{y}_4(t) \\ \dots \\ \dot{y}_{n-2}(t) - \dot{y}_{n-1}(t) \\ \dot{y}_{n-1}(t) - \dot{y}_n(t) \end{pmatrix} = \begin{pmatrix} 0 \\ 0 \\ \dots \\ 0 \end{pmatrix} \quad (8)$$

Without considering the damping force, the mechanical expression for the i th mass block in the x and y directions can be obtained by substituting Equations (3), (5), and (6) into Equations (2) and (4) respectively.

$$m_i \ddot{x}_i(t) + \left\{ \begin{array}{l} b_{i-1,0} + b_{i-1,1} [\sqrt{[x_i(t) - x_{i-1}(t)]^2 + [y_i(t) - y_{i-1}(t)]^2} - \sqrt{[x_i(0) - x_{i-1}(0)]^2 + [y_i(0) - y_{i-1}(0)]^2}] \\ + b_{i-1,2} [\sqrt{[x_i(t) - x_{i-1}(t)]^2 + [y_i(t) - y_{i-1}(t)]^2} - \sqrt{[x_i(0) - x_{i-1}(0)]^2 + [y_i(0) - y_{i-1}(0)]^2}] + \dots + \\ b_{i-1,q} [\sqrt{[x_i(t) - x_{i-1}(t)]^2 + [y_i(t) - y_{i-1}(t)]^2} - \sqrt{[x_i(0) - x_{i-1}(0)]^2 + [y_i(0) - y_{i-1}(0)]^2}]^q \end{array} \right\} \frac{x_{i-1}(t) - x_i(t)}{\sqrt{[x_i(t) - x_{i-1}(t)]^2 + [y_i(t) - y_{i-1}(t)]^2}} \\ + \left\{ \begin{array}{l} b_{i,0} + b_{i,1} [\sqrt{[x_{i+1}(t) - x_i(t)]^2 + [y_{i+1}(t) - y_i(t)]^2} - \sqrt{[x_{i+1}(0) - x_i(0)]^2 + [y_{i+1}(0) - y_i(0)]^2}] \\ + b_{i,2} [\sqrt{[x_{i+1}(t) - x_i(t)]^2 + [y_{i+1}(t) - y_i(t)]^2} - \sqrt{[x_{i+1}(0) - x_i(0)]^2 + [y_{i+1}(0) - y_i(0)]^2}] + \dots + \\ b_{i,q} [\sqrt{[x_{i+1}(t) - x_i(t)]^2 + [y_{i+1}(t) - y_i(t)]^2} - \sqrt{[x_{i+1}(0) - x_i(0)]^2 + [y_{i+1}(0) - y_i(0)]^2}]^q \end{array} \right\} \frac{x_i(t) - x_{i+1}(t)}{\sqrt{[x_{i+1}(t) - x_i(t)]^2 + [y_{i+1}(t) - y_i(t)]^2}} = 0 \quad (9)$$

$$m_i \ddot{y}_i(t) + \left\{ \begin{array}{l} b_{i-1,0} + b_{i-1,1} [\sqrt{[x_i(t) - x_{i-1}(t)]^2 + [y_i(t) - y_{i-1}(t)]^2} - \sqrt{[x_i(0) - x_{i-1}(0)]^2 + [y_i(0) - y_{i-1}(0)]^2}] \\ + b_{i-1,2} [\sqrt{[x_i(t) - x_{i-1}(t)]^2 + [y_i(t) - y_{i-1}(t)]^2} - \sqrt{[x_i(0) - x_{i-1}(0)]^2 + [y_i(0) - y_{i-1}(0)]^2}] + \dots + \\ b_{i-1,q} [\sqrt{[x_i(t) - x_{i-1}(t)]^2 + [y_i(t) - y_{i-1}(t)]^2} - \sqrt{[x_i(0) - x_{i-1}(0)]^2 + [y_i(0) - y_{i-1}(0)]^2}]^q \end{array} \right\} \frac{y_i(t) - y_{i-1}(t)}{\sqrt{[x_i(t) - x_{i-1}(t)]^2 + [y_i(t) - y_{i-1}(t)]^2}} \\ + \left\{ \begin{array}{l} b_{i,0} + b_{i,1} [\sqrt{[x_{i+1}(t) - x_i(t)]^2 + [y_{i+1}(t) - y_i(t)]^2} - \sqrt{[x_{i+1}(0) - x_i(0)]^2 + [y_{i+1}(0) - y_i(0)]^2}] + b_{i,2} \\ [\sqrt{[x_{i+1}(t) - x_i(t)]^2 + [y_{i+1}(t) - y_i(t)]^2} - \sqrt{[x_{i+1}(0) - x_i(0)]^2 + [y_{i+1}(0) - y_i(0)]^2}] + \dots + b_{i,q} \\ [\sqrt{[x_{i+1}(t) - x_i(t)]^2 + [y_{i+1}(t) - y_i(t)]^2} - \sqrt{[x_{i+1}(0) - x_i(0)]^2 + [y_{i+1}(0) - y_i(0)]^2}]^q + c_i [\dot{x}_i(t) - \dot{x}_{i+1}(t)] \end{array} \right\} \frac{y_i(t) - y_{i+1}(t)}{\sqrt{[x_{i+1}(t) - x_i(t)]^2 + [y_{i+1}(t) - y_i(t)]^2}} = 0 \quad (10)$$

Equations (9) and (10) demonstrate the motion of a mass block located on the random position of the screen plate, excluding the mass blocks situated at the two end positions, is a nonlinear superposition of the motion responses of the mass blocks at the remaining positions.

3. Experiments

3.1. Acceleration Testing at the Midpoint of the Screen Plate

Figure 6 shows an acceleration testing platform, which consists of a FFSP experimental system (motor, transmission device, crank link system, moving beam, FFSP, fixed beam) and a data acquisition system (acceleration sensor, data acquisition instrument, laptop). As shown in Figure 7, the acceleration sensor is fixed at the midpoint of the screen plate.

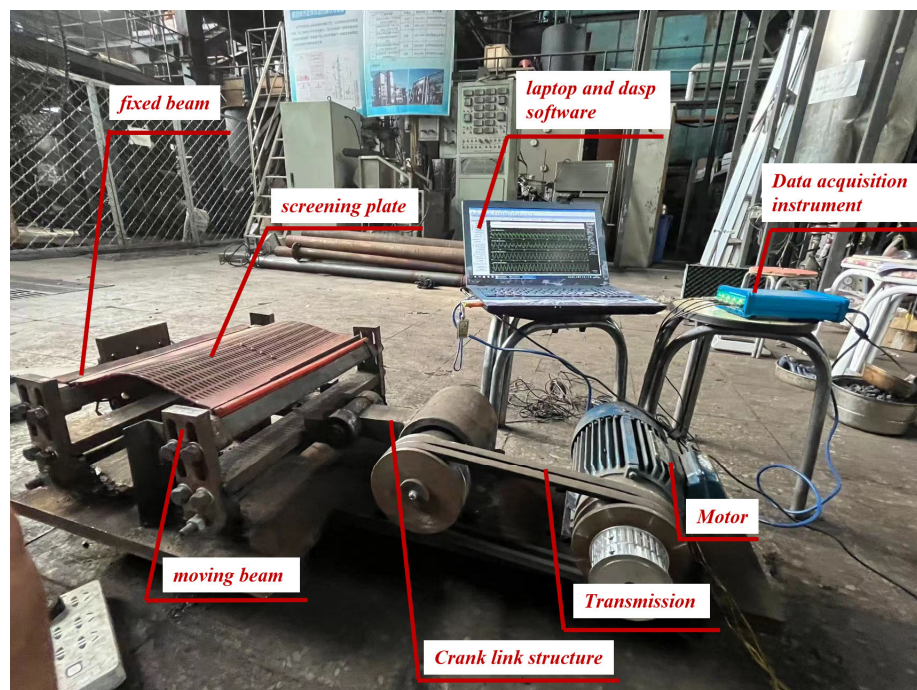


Figure 6. Acceleration testing platform for FFSP.

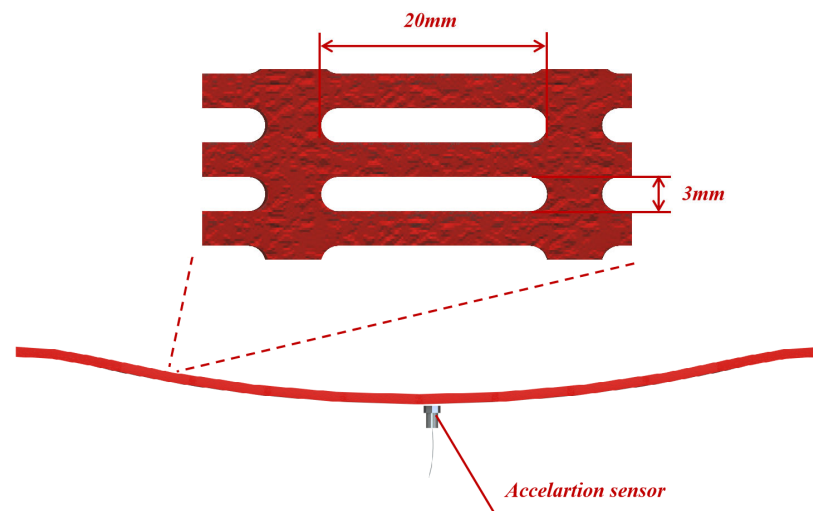


Figure 7. Flip-flow screen plate.

The working process is as follows: First, start the motor, which in turn leads to the motion of the crank link system through the transmission device. Then, the moving beam connected to the crank link system produces periodic motion with an amplitude of 6.8 mm. The periodic motion of the moving beam leads to the FFSP undergoing alternating relaxed and tightening reciprocating motion. During the motion of the screen plate, the acceleration sensor fixed at the midpoint of the screen directly measures the acceleration at the midpoint of the screen surface. The signal is collected by the data acquisition instrument and uploaded to the DASP software on the laptop for recording and analysis.

Equation (1) demonstrates that there are two methods to adjust the PSA of the screen plate under the condition of a fixed amplitude: by modifying the arc length of the screen plate or adjusting the spacing of the beams in a static equilibrium state.

In this study, we modify the PSA of the flip-flow screen plate by adjusting the position of the fixed pendulum rod to alter the spacing of beams. The arc length (L) of the screen plate in this study is 328 mm. We adjusted the beam spacing to 328 mm, 325 mm, 322 mm, 319 mm, and 316 mm in the condition of static equilibrium, which correspond to PSAs of 0 mm, -3 mm, -6 mm, -9 mm, and -12 mm, respectively. When the PSA (Δl) was greater than or equal to $-A$, the screen plate underwent a progress of being stretched tightly during movement; When Δl was less than $-A$, the screen plate remained in a relaxed state throughout. The key of data recording was activated to record the acceleration signal at each PSA after the FFSP was operating steadily.

3.2. Screening Experiment of the FFSP

After the motion test of the FFSP with varying PSAs, this study explores the impact of the PSA on the screening efficiency of the screen plate. A screening experimental platform is constructed as illustrated in Figure 8. The screening experimental platform is composed of two parts: the transmission component and the screening component. In this study, a screen plate with straight slotted holes measuring 3 mm \times 20 mm is employed for the screening process and the size of the sieve holes is shown in Figure 7. The PSA mentioned in Section 3.1 is applied during the screening.

The coal used in this experiment for investigation is bituminous coal from Yangcheng, Shanxi, China. Before conducting the experiments, the coal samples were first subjected to particle size analysis. Using sieves with apertures of 0.25 mm, 1 mm, 3 mm, 4.75 mm, 13 mm, and 25 mm, the dried coal samples were sieved to obtain the particle size distribution of the raw coal.

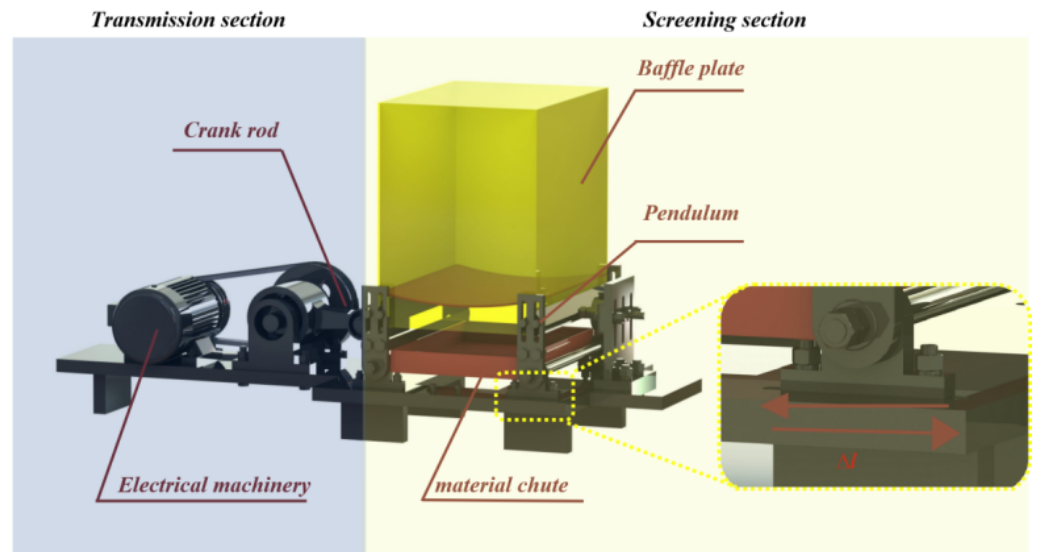


Figure 8. Screening Experiment for a FFSP.

The particle size distribution of this raw coal is shown in Figure 9. It can be observed that the experimental coal consists of seven particle size grades, namely, +25 mm, 13–25 mm, 4.75–13 mm, 3–4.75 mm, 1–3 mm, 0.25–1 mm, and –0.25 mm. In Figure 9, the cumulative curve moves upward and to the right, indicating a higher content of coarse particles in the material. The main particle sizes are +25 mm, 13–25 mm, and 4.75 mm–13 mm, accounting for 34.02%, 26.06%, and 23.31% of the total, respectively. The particle size grade of 3–4.75 mm represents 6.8% of the total mass, while the particle size grade of –3 mm account for 9.73% of the total mass. Additionally, the moisture content of the material in this experiment is 5.87%.

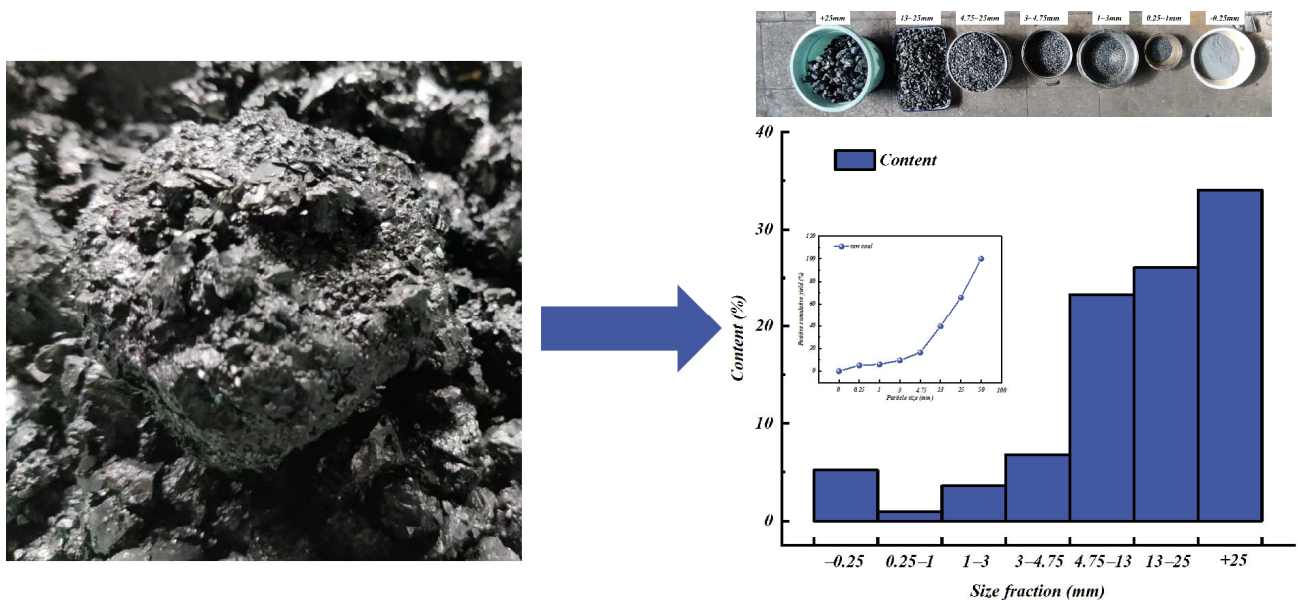


Figure 9. The grain size composition of raw coal.

After the analysis of the grain size composition of the raw coal, 3.5 kg of raw coal was placed on the FFSP and screened. According to the research by Zhao [23], the average velocity of particles of different particle sizes along the material flow direction on the FFS is between 0.5–1.2 m/s. Based on this conclusion, it would take 24 s for all materials to pass through a 12 m long FFS. To better approximate the actual screening

process, a screening time of 25 s is therefore used to represent the passage time of all materials on the screening machine.

Then we changed the PSAs of the screen plate to -12 mm, -9 mm, -6 mm, -3 mm, 0 mm, respectively and repeat the operations above. Finally, the screening efficiency and misplaced content of oversized particles were analyzed under different conditions.

3.3. Evaluation of Screening Performance

The screening efficiency and misplaced content of coarse particles are used to evaluate the screening performance in this paper, which are calculated as Equations (11), (12) and (13), respectively [45,46].

$$\eta = E_c + E_f - 100 \quad (11)$$

$$\begin{cases} E_c = \frac{\gamma_o \times O_c}{F_c^r} \times 100 \\ E_c = \frac{F_f^r - \gamma_o \times O_c}{F_f^r} \times 100 \end{cases} \quad (12)$$

$$\begin{cases} M_O = M_c + M_f \\ M_c = \gamma_u U_c \times 100 \\ M_f = \gamma_o O_f \times 100 \end{cases} \quad (13)$$

where η represents the screening efficiency, determined by E_c (%) and E_f (%); E_c denotes the effective placement efficiency of coarse particles, E_f denotes the effective placement efficiency of fine particles. M_o (%) stands for the total misplaced materials; M_c (%) represents the misplaced materials of coarse particles, and M_f (%) represents the misplaced materials of fine particles. γ_o (%) indicates the oversized product yield, while γ_u (%) represents the undersized product yield. O_f (%) denotes the ratio of fine particles in the oversized product, O_c (%) denotes the ratio of coarse particles in the oversized product. F_c^r (%) represents the ratio of coarse particles in the feed, and F_f^r (%) represents the ratio of fine particles in the feed.

4. Results and Discussion

In this section, a detailed analysis of the acceleration signals at the midpoint of the FFSP obtained from experiments is conducted, and the calculation of the nonlinear stiffness coefficient of the FFSP in the vertical direction under this experimental condition is performed. The results indicate that under this experimental condition, the mechanical model of the FFSP can be simplified to a nonlinear spring-tri-body model, with the calculation error of the simplified mechanical model being within 30%. Subsequently, the changes in the motion status of the FFSP resulting from variations in the PSA are discussed in conjunction with the experimental data. Finally, the impact of PSA variations on the screening efficiency of coal is explored, analyzing the influence of PSA changes on the screening efficiency from the perspectives of screen plate acceleration and motion status.

4.1. Analysis of Acceleration Signals

4.1.1. The Result of the Acceleration Testing at the Midpoint of FFSP

The acceleration signals at the midpoint of the screen plate under 5 different PSAs obtained in the experiment are shown in Figure 10. Figure 10a–e respectively illustrate the curves of the acceleration variation over time at the midpoint of the screen plate along the direction perpendicular to the screen plate under PSAs of -12 mm, -9 mm, -6 mm, -3 mm, and 0 mm.

According to the results shown in Figure 10, under this experimental condition, when the PSA is -12 mm, the acceleration of the screen plate fluctuates within the range of $[-41$ g, 25.5 g]; when the PSA is -9 mm, the acceleration of the screen plate fluctuates within the range of $[-67.5$ g, 50.8 g]; when the PSA is -6 mm, the acceleration of the screen plate fluctuates within the range of $[-101$ g, 53.6 g]; when the PSA is -3 mm, the acceleration of the screen plate fluctuates within the range of $[-52.6$ g, 66.7 g]; when

the PSA is 0 mm, the acceleration of the screen plate fluctuates within the range of $[-51.4 \text{ g}, 85.8 \text{ g}]$.

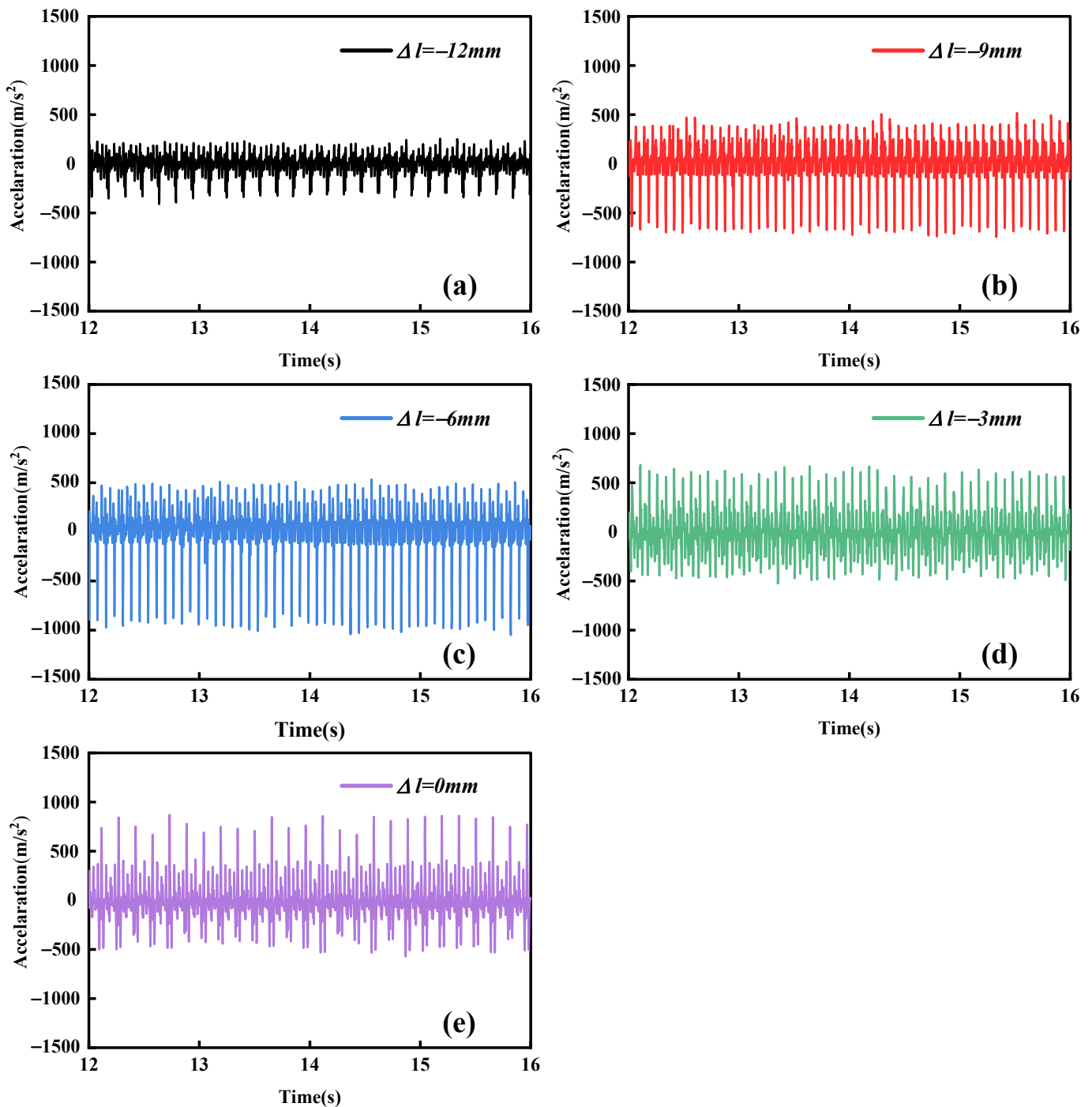


Figure 10. The result of the acceleration testing at the midpoint of the screen plate.

As shown in Figure 11, a curve of the peak value of the acceleration at the midpoint of the FFSP varies the PSA is plotted. There are two curves in Figure 11: the black curve illustrates the relationship between the peak value of the acceleration upward perpendicular to the screen plate and the PSA. It can be observed that, as the PSA changes from -12 mm to 0 mm , the peak acceleration upward perpendicular to the screen plate shows a monotonically increasing trend, gradually increasing from 25.5 g to 85.5 g .

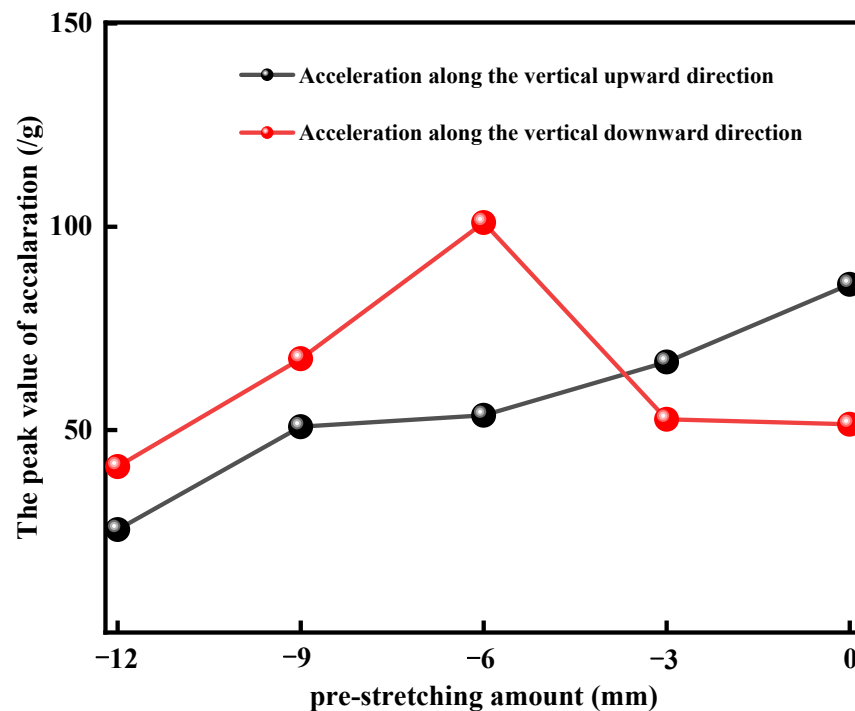


Figure 11. The peak value of the acceleration at the midpoint of the FFSP varies the PSA.

The red curve depicts the relationship between the peak acceleration downward perpendicular to the screen plate and the PSA. It is evident that during the process of PSA varying from -12 mm to 0 mm, the downward acceleration peak first changes from 41 g to 101 g, then sharply drops to 52.6 g, and finally returns to 51.4 g.

Based on the experimental data from Figures 10 and 11, the following conclusions can be drawn: when the PSA is less than or equal to -6 mm (indicating the screen plate is fully relaxed during the stretching relaxation motion), the peak acceleration in the vertical upward direction is less than the peak acceleration in the vertical downward direction. On the other hand, when the PSA is greater than -6 mm (indicating the screen plate is being tightened during the motion), the peak acceleration in the vertical upward direction is greater than the peak acceleration in the vertical downward direction.

Of particular note is that at a PSA of -6 mm, the magnitude of acceleration along the vertical direction upward is close to half of the acceleration magnitude downward.

4.1.2. Analyzation of the PSD

To further investigate the influence of PSA on the acceleration of the FFSP, this section explores the energy distribution of the motion at the midpoint of the screen along the frequency domain, power spectral density [36,47,48] analysis of the acceleration signals of the screen plate under different PSAs is conducted, as shown in Figure 12.

Figure 12 illustrates the power of the acceleration signal carried by each unit frequency wave. According to Figure 12, the range of the frequency domain corresponding to the energy distribution of the acceleration signal is 0 – 169 Hz under an external excitation frequency of 13 Hz. This indicates that the energy distribution of the acceleration signal at the midpoint of the screen is relatively dispersed along the frequency domain, which is caused by the non-linear characteristics of the screen plate.

Different PSAs produce varying degree of energy dispersion along the frequency domain. The peak value of the PSD of the acceleration signals at the midpoint of the screen with a PSA of -12 mm is not significant.

The screen plate with a PSA of -9 mm features two high-energy peaks in the PSD of the acceleration signal and these two peaks correspond to the external excitation frequency and the triplex of the external excitation frequency, respectively.

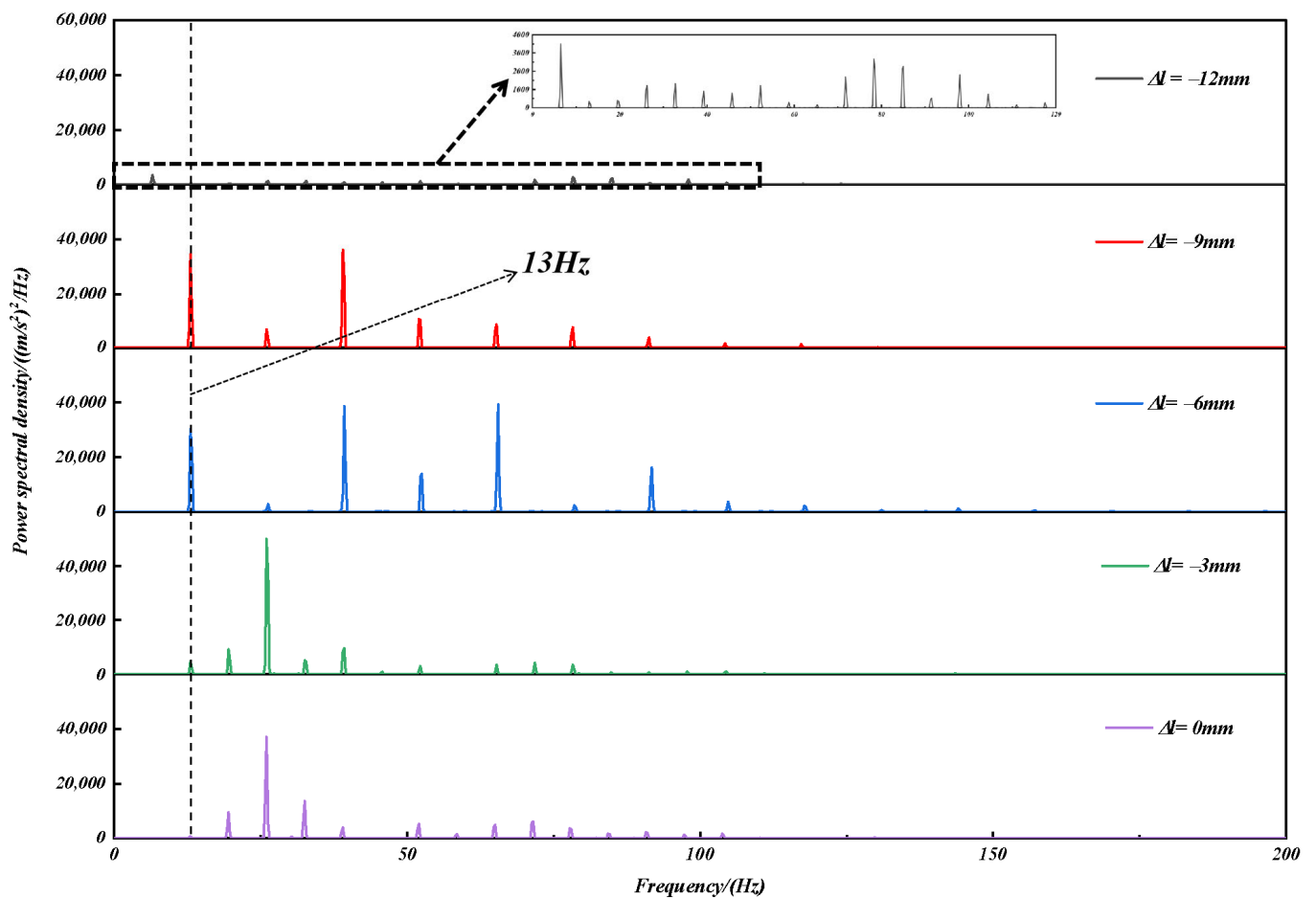


Figure 12. PSD analysis of acceleration signals under different PSAs.

The power spectral density (PSD) of the acceleration signals of the screen plate with a PSA of -6 mm reveals three peak values which are the single, triple, and quintuple of the external excitation frequency, respectively.

The power spectral density (PSD) of the acceleration signals of the screen plate with PSA of -3 mm and 0 mm both exhibit one peak, which corresponds to twice of external excitation frequency.

These suggests that the degree of concentration of energy distribution along the frequency domain changes by the change of the PSA. The screen plate with a PSA of -12 mm shows the most dispersed power distribution across the frequency domain. In general, as the PSA increases, the degree of concentration of energy distribution along the frequency domain also increases.

Moreover, the fundamental frequency of the acceleration signal under different PSAs is not always consistent with the excitation frequency. This observation further confirms the varying density of peak accelerations of the screen plate under different PSAs, as depicted in Figure 10. The PSD of the acceleration signal at the midpoint of the screen plate, with a PSA of -12 mm, demonstrates a fundamental frequency that is half of the frequency of excitation signal; The fundamental frequency of the acceleration signal at the midpoint of the screen plate equals to the frequency of excitation signal for PSA of -9 mm and -6 mm; Nevertheless, when the PSA changes to -3 mm or 0 mm, the fundamental frequency of the signal returns to being half of the frequency of excitation signal.

In summary, the degree of concentration of energy distribution across the frequency domain increases as the PSA changes from -12 mm to 0 mm. Additionally, the fundamental frequency of the screen plate does not always coincide with the frequency of the excitation signal when the PSA varies.

4.1.3. Nonlinear Spring-Tri-Body Model

To simplify the calculations, the nonlinear spring-multi-body model is simplified to the nonlinear spring-tri-body model shown in Figure 13, where mass block m_3 represents the end of the screen plate connected to the fixed rod, and mass block m_1 represents the end of the screen plate connected to the moving beam. Given that the motion perpendicular to the FFSP’s midpoint during the screening process is significantly greater than the motion in other directions [37], this study disregards the motion of the screen plate in the remaining directions. Thus, the formula $x_2(t) = x_2(0)$ can be obtained. The equation (10) of motion for the midpoint of the screen plate in the direction perpendicular to the screen plate can be reformulated as Equation (14):

$$m_2 \ddot{y}_2(t) + \left\{ \begin{aligned} & b_{1,0} + b_{1,1} [\sqrt{[x_2(0) - x_1(t)]^2 + [y_2(t) - y_1(t)]^2} - \sqrt{[x_2(0) - x_1(0)]^2 + [y_2(0) - y_1(0)]^2}] \\ & + b_{1,2} [\sqrt{[x_2(0) - x_1(t)]^2 + [y_2(t) - y_1(t)]^2} - \sqrt{[x_2(0) - x_1(0)]^2 + [y_2(0) - y_1(0)]^2}]^2 + \dots + \\ & b_{1,q} [\sqrt{[x_2(0) - x_1(t)]^2 + [y_2(t) - y_1(t)]^2} - \sqrt{[x_2(0) - x_1(0)]^2 + [y_2(0) - y_1(0)]^2}]^q \end{aligned} \right\} \frac{y_2(t) - y_1(t)}{\sqrt{[x_2(0) - x_1(t)]^2 + [y_2(t) - y_1(t)]^2}} \\ + \left\{ \begin{aligned} & b_{2,0} + b_{2,1} [\sqrt{[x_3(t) - x_2(0)]^2 + [y_3(t) - y_2(t)]^2} - \sqrt{[x_3(0) - x_2(0)]^2 + [y_3(0) - y_2(0)]^2}] + b_{2,2} \\ & [\sqrt{[x_3(t) - x_2(0)]^2 + [y_3(t) - y_2(t)]^2} - \sqrt{[x_3(0) - x_2(0)]^2 + [y_3(0) - y_2(0)]^2}]^2 + \dots + b_{2,q} \\ & [\sqrt{[x_3(t) - x_2(0)]^2 + [y_3(t) - y_2(t)]^2} - \sqrt{[x_3(0) - x_2(0)]^2 + [y_3(0) - y_2(0)]^2}]^q \end{aligned} \right\} \frac{y_2(t) - y_3(t)}{\sqrt{[x_3(t) - x_2(0)]^2 + [y_3(t) - y_2(t)]^2}} = 0 \tag{14}$$

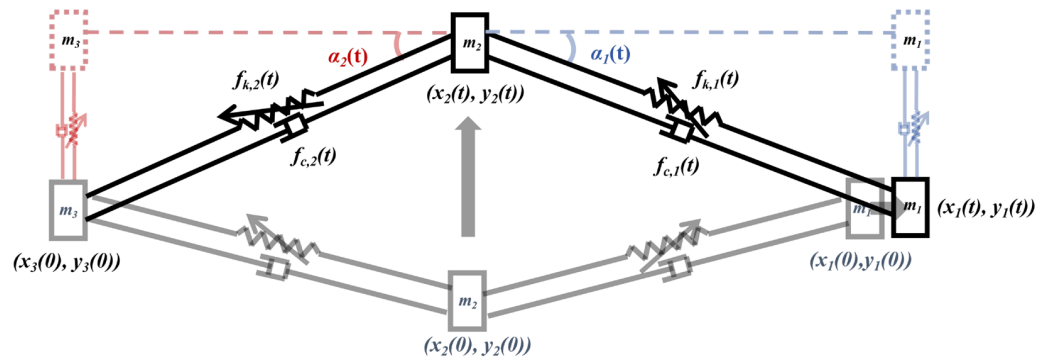


Figure 13. Nonlinear spring-tri-body model.

In Equation (14), the positions of the mass blocks m_1 and m_3 located at the ends of the screen plate can be expressed as:

$$\begin{cases} x_1(t) = a + A_{rx} \sin \omega t \\ y_1(t) = A_{ry} \sin \omega t \\ x_3(t) = A_{lx} \sin \omega t \\ y_3(t) = A_{ly} \sin \omega t \end{cases} \tag{15}$$

In Equation (15), a represents the initial horizontal distance (beam spacing) in mm between mass block 1 and mass block 3 of the screen plate; A_{rx} denotes the amplitude in mm of the floating beam in the horizontal direction; A_{ry} represents the amplitude in mm of the floating beam in the vertical direction; A_{lx} signifies the amplitude in mm of the moving beam in the horizontal direction; and A_{ly} stands for the amplitude in mm of the moving beam in the vertical direction.

By substituting the experimentally measured acceleration data of the midpoint of the FFSP from Figure 10 into Equation (14) and performing calculations using MATLAB software, the non-linear spring tri-body model can yield the non-linear stiffness coefficients b_0, b_1, \dots, b_9 along the direction perpendicular to the screen plate for 5 different PSAs, as shown in Table 1. Table 1 indicates that variations in PSA lead to changes in the non-linear stiffness coefficient of the FFSP.

The comparison between the calculated value of the acceleration under different PSAs obtained from the non-linear spring-tri-body model and the experimental data is shown in Figure 14.

Table 1. Calculation value of Non-linear Stiffness Coefficients along the Vertical Direction at the midpoint of the FFSP.

$\Delta l/mm$	b_0 (N)	b_1 (N/m)	b_2 (N/m ²)	b_3 (N/m ³)	b_4 (N/m ⁴)	b_5 (N/m ⁵)	b_6 (N/m ⁶)	b_7 (N/m ⁷)	b_8 (N/m ⁸)	b_9 (N/m ⁹)
-12	-548.988	-37,640.92	9,568,491.077	-1.32×10^8	-4.297×10^{10}	8.047×10^{11}	8.16×10^{13}	-1.33×10^{15}	-5.18×10^{16}	7.632×10^{17}
-9	-865.213	102,751.12	23,203,798.61	-3.371×10^8	-1.5386×10^{11}	-1.659×10^{12}	5.53×10^{14}	-2.467×10^{14}	-7.469×10^{17}	1.26×10^{19}
-6	-98.5136	204,353.7	17,901,293.79	-1.126×10^8	-1.001×10^{11}	2.622×10^{12}	2.278×10^{14}	-5.027×10^{15}	-1.78×10^{17}	3.90×10^{18}
-3	-542.3882	-108,175.29	-9,989,635.331	1.9163×10^8	2.395×10^{11}	-1.099×10^{13}	-1.097×10^{15}	1.404×10^{16}	1.468×10^{18}	5.98×10^{18}
0	-699.191	-126,391.67	27,327,389.79	2.5388×10^8	-1.75×10^{11}	-1.897×10^{13}	6.345×10^{14}	3.9×10^{16}	-7.787×10^{17}	-2.33×10^{19}

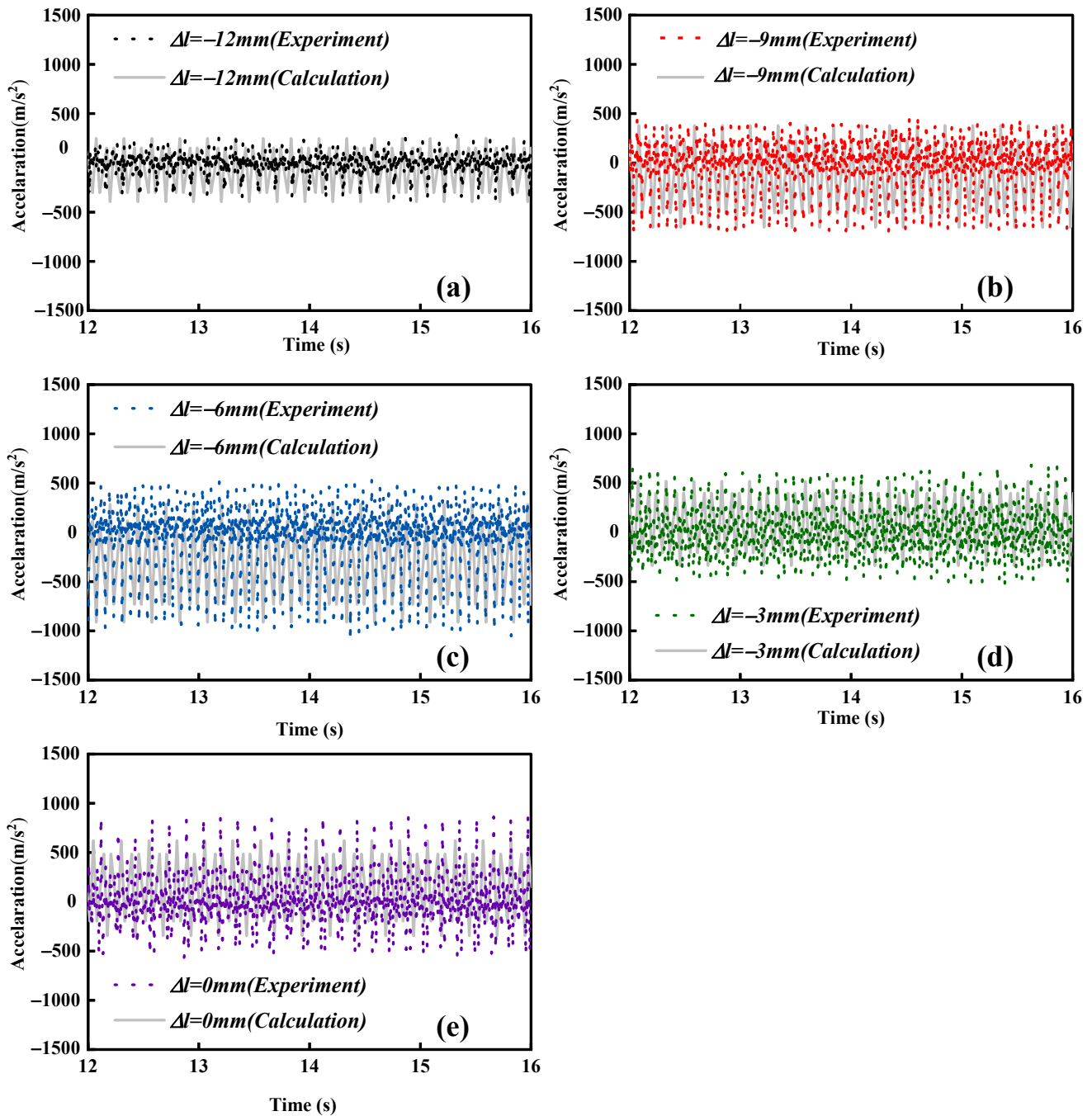


Figure 14. The comparison between the calculated value of the acceleration and the experimental data under different PSAs.

Figure 14a–e display the comparison between the experimental values and the calculated values of the acceleration time graph in the vertical direction of mass block m_2 after being subjected to periodic excitation for different PSAs of the screen plate ($\Delta l = -12$ mm, -9 mm, -6 mm, -3 mm, 0 mm) in the non-linear spring-tri-body model.

Table 2 displays the errors between the experimental values and the calculated values obtained by using the nonlinear spring-tri-body model. From Table 2, it can be inferred that with known non-linear stiffness coefficients of the screen plate, the errors in the calculation results using the nonlinear spring-tri-body model are within 30%. Therefore, the non-linear spring-tri-body model can effectively approximate the mechanical model of the FFSP under the experimental conditions.

Table 2. Error value between calculation and experiment.

$\Delta l/\text{mm}$	-12	-9	-6	-3	0
Error value/%	7.69	14.61	19.67	25.09	26.5

4.2. The Effect of Various PSAs on Motion State of the Screen Plate

The phase diagram and Poincaré mapping [38] are plotted for the midpoint of the flip-flow screen plate under different PSAs. The vertical co-ordinate is the velocity at the midpoint position of the screen plate, while the displacement of the midpoint of the screen plate is used for the horizontal coordinate. The results are presented in Figures 15–19.

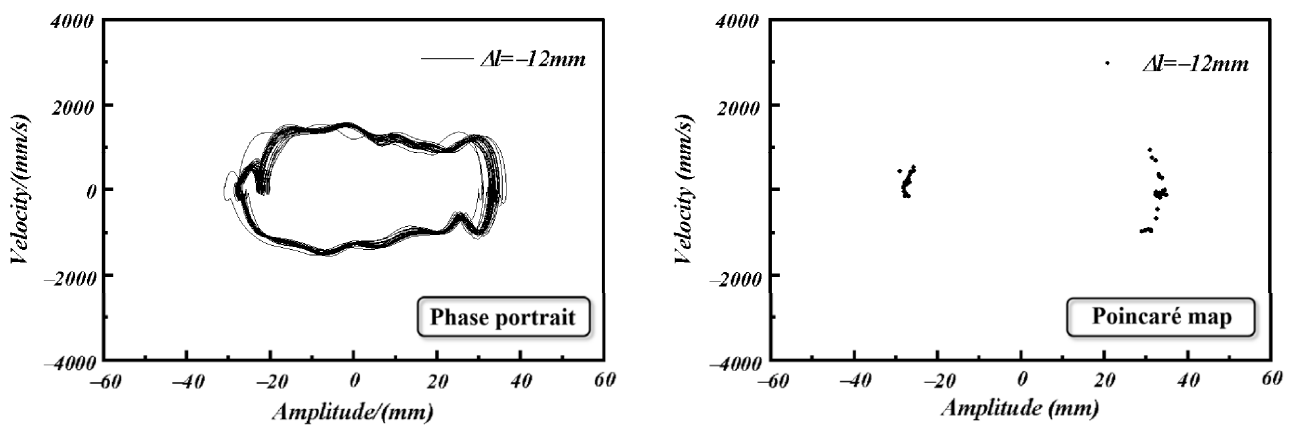


Figure 15. Phase diagram and Poincaré mapping of the midpoint of the screen plate ($\Delta l = -12$ mm).

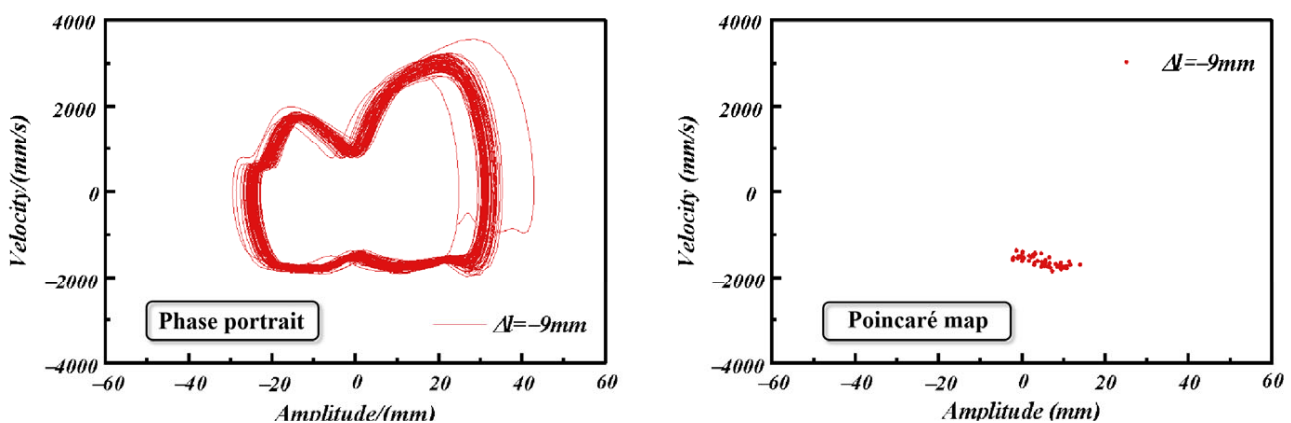


Figure 16. Phase diagram and Poincaré mapping of the midpoint of the screen plate ($\Delta l = -9$ mm).

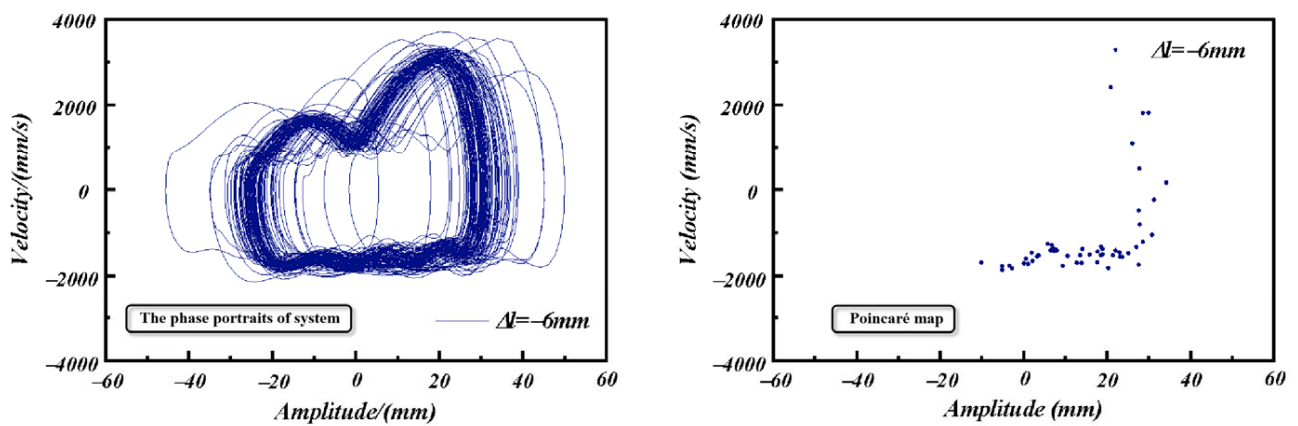


Figure 17. Phase diagram and Poincaré mapping of the midpoint of the screen plate ($\Delta l = -6$ mm).

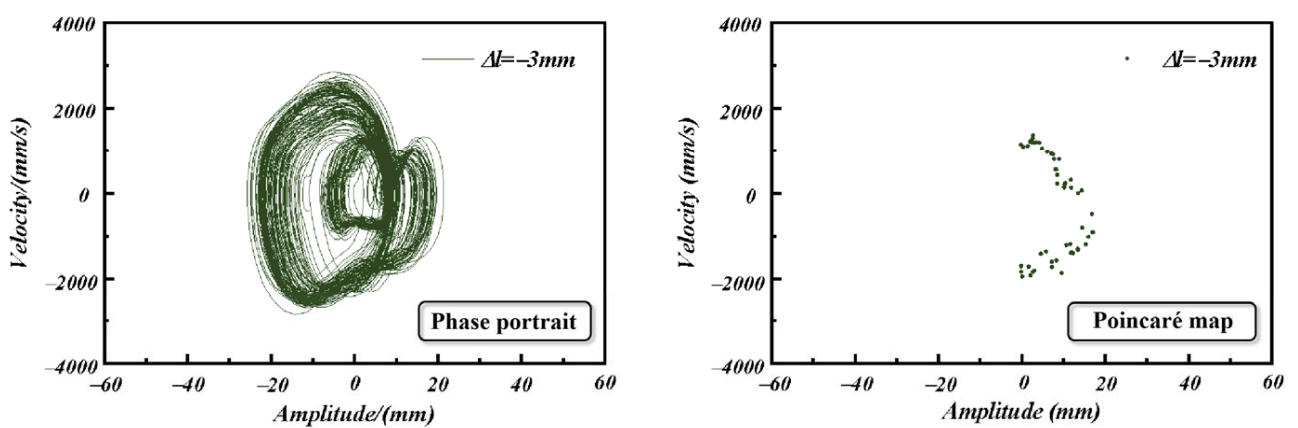


Figure 18. Phase diagram and Poincaré mapping of the midpoint of the screen plate ($\Delta l = -3$ mm).

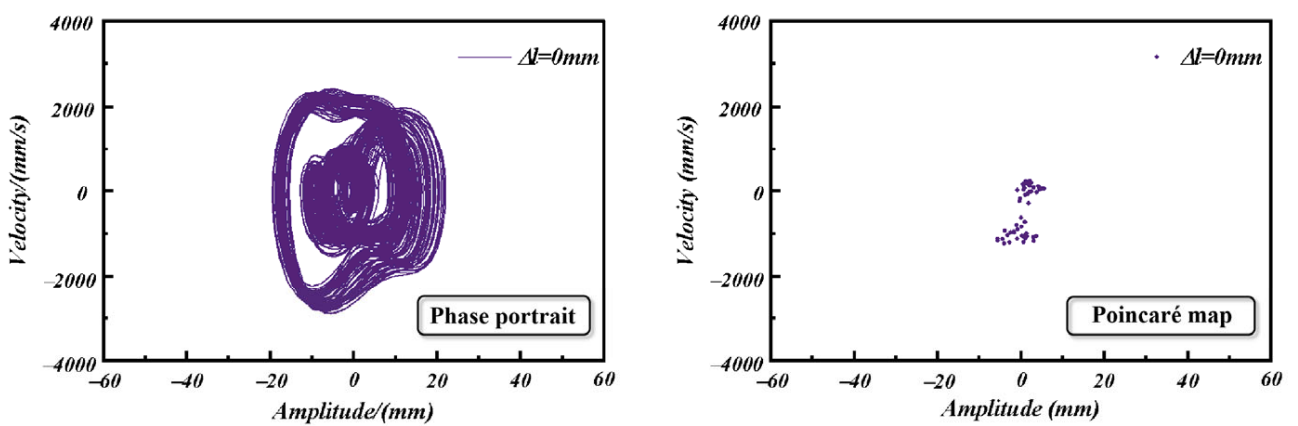


Figure 19. Phase diagram and Poincaré mapping of the midpoint of the screen plate ($\Delta l = 0$ mm).

The midpoint of FFSP with a PSA of -12 mm exhibit cyclic phase trajectories that do not overlap into a single ring. The Poincaré mapping diagram demonstrates multiple clusters consists of dense points. As a result, the motion state of the midpoint of the screen plate under this amount of pre-stretching is quasi-periodic.

Under a PSA of -9 mm, the phase trajectory is composed of multiple loops with cyclic characteristics overlapping each other. In this state, the disorderliness of the phase trajectory slightly increases, but the Poincaré map shows a cluster of dense point set images. Therefore, under this condition, the motion state of the midpoint on the screen plate still remains in quasi-periodic motion.

Under a PSA of -6 mm, although the phase trajectory is also composed of multiple overlapping loops, the disorderliness is the strongest compared to other conditions. In Figure 17, it can be observed in the phase diagram that the non-coincidence of the phase trajectory is higher. The Poincaré map exhibits a hierarchical scatter distribution pattern, indicating that the system is closer to a chaotic motion state under this condition.

Under a PSA of -3 mm, the phase trajectory is composed of multiple non-overlapping loops, making the phase trajectory more complex. However, compared to the phase trajectory under a PSA of -6 mm, the degree of disorderliness has significantly declined. The scatter plot in the Poincaré map shows a more clustered trend compared to Figure 17, indicating that under this condition, the motion state of the midpoint on the screen plate is closer to a quasi-periodic motion state.

Under a PSA of 0 mm, the phase trajectory is composed of multiple intertwining and overlapping curves of different sizes. Compared to the phase trajectory under a PSA of -3 mm, the concentration of the phase trajectories is higher under this condition, and the degree of disorderliness declines again. Additionally, the Poincaré map exhibits multiple clustered point patterns, indicating that the motion of the midpoint on the FFSP under this condition is quasi-periodic.

During the process of PSA changing from -12 mm to 0 mm, the degree of the disorderliness of the phase trajectory first increases and then decreases. The Poincaré map transitions from dense clustered point patterns to a hierarchical scatter distribution pattern and then to multiple clusters of dense point patterns. This indicates that the motion of the midpoint on the screen plate transitions from a quasi-periodic state to a transitional state from quasi-periodic to chaotic, and finally returns to quasi-periodic motion.

Furthermore, with -6 mm PSA as the threshold, the complexity of the phase trajectory with PSAs greater than -6 mm is higher than that of the phase trajectory with PSAs less than -6 mm. This may be related to the fact that screens with PSAs greater than -6 mm exhibit a tightened state during periodic motion.

4.3. The Influence of PSA on the Screening Efficiency

In this study, the misplaced content of oversized particles [49] along with the screening efficiency of particles are employed to evaluate the screening performance of the screen plates under different PSAs. Figure 20 illustrates the variations in the misplaced content of oversized particles and screening efficiency of particles as the PSA varies from -12 mm to 0 mm.

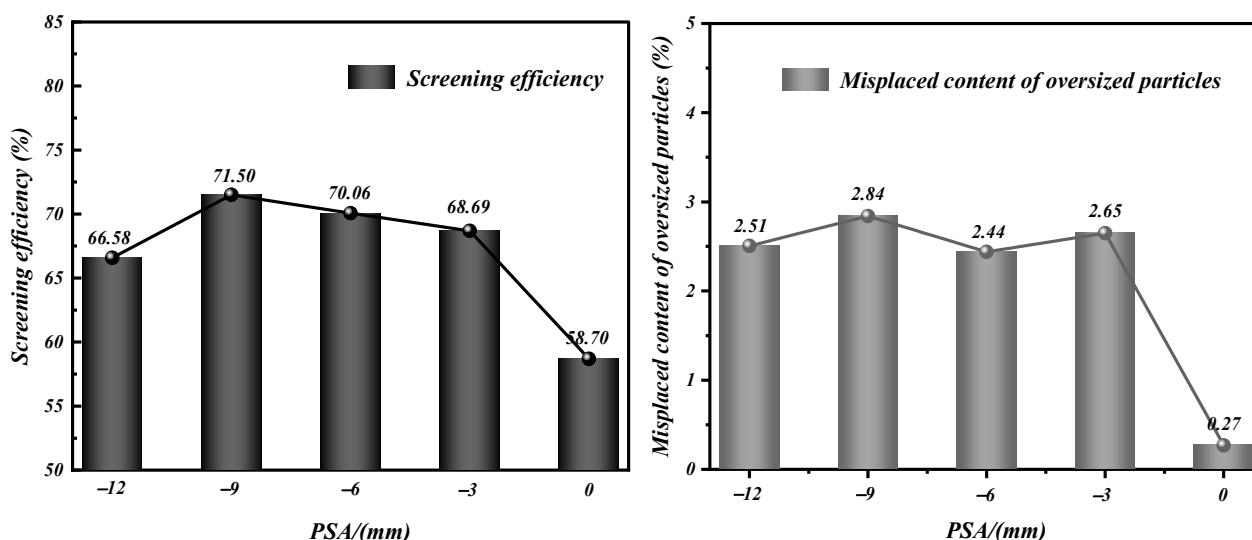


Figure 20. Impact of PSA on screening performance.

According to Figure 20, as the PSA increases from -12 mm to -9 mm, the screening efficiency improves by 4.92%. Subsequently, between the PSAs of -9 mm and -3 mm, the screening efficiency exhibits small fluctuations within a range of 3%. Finally, as the PSA changes from -3 mm to 0 mm, the screening efficiency decreases by 9.99%. The misplaced content of oversized particles fluctuates within 0.4% in the PSA range of -12 mm to -3 mm, but sharply drops by 2.38% at the 0 mm PSA.

From Figure 20, it can be seen that the screening efficiency reaches its maximum at -9 mm, and there is no significant fluctuation within the PSA range of $[-9$ mm, -3 mm]. At this point, the motion state of the screen is in the vicinity of the transitional state from quasi-periodic to chaotic motion.

Furthermore, by comparing Figure 11 (The peak value of the acceleration at the midpoint of the FFSP varies the PSA) with Figure 20, we seem to observe an interesting phenomenon: When the upward acceleration amplitude is less than 50.8 g, the screening efficiency increases with the increasing of the acceleration of the screen plate; however, when the acceleration amplitude exceeds 50.8 g, the screening efficiency gradually decreases with the increasing of the acceleration.

It is worth noting that when the value of PSA exceeding -9 mm, the change trend of screening efficiency PSA curve is exactly opposite to the acceleration PSA curve, and the rate of change of these two curves tends to be consistent. In addition, there is no apparent correlation between the screening efficiency and the amplitude of acceleration perpendicular to the screen plate pointing downwards. Therefore, we can conclude that the screening efficiency is mainly affected by the acceleration amplitude perpendicular to the screen plate pointing upwards, and the suitable acceleration for the material in the study is approximately around 50.8 g.

For misplaced content of oversized particles, within the range of -12 mm to -3 mm, although there are fluctuations, the change is not significant, remaining within 0.4%. However, at a PSA of 0 mm, the misplaced content of oversized particles shows a sharp downward trend, dropping suddenly by 2.38%.

By comparing the misplaced content of oversized particles with the acceleration PSA curve and the motion status of the screen plate, it is found that the change in misplaced content of oversized particles is not dependent on the motion status of the screen plate, nor is it significantly associated with the magnitude of the acceleration perpendicular to the screen plate pointing downward. In fact, the main factor affecting the misplaced content of oversized particles is the acceleration amplitude of the screen plate in the vertical direction pointing upward. When the vertical upward acceleration amplitude is less than or equal to 66.7 g, the effect of PSA on the misplaced content of oversized particles is not significant. However, when the acceleration amplitude of the screen plate along the vertical direction pointing upward increases to 101 g, the misplaced content of oversized particles drops sharply, indicating a significant reduction in the collision frequency between coarse particles and the screen plate.

In conclusion, the screening efficiency and the misplaced content of oversized particles are only related to the acceleration amplitude along the vertical direction pointing upward of the screen plate, and are not related to the motion status of the screen plate or the acceleration magnitude along the vertical direction pointing downward. The appropriate range for pre-stretch value in this study is $[-9$ mm, -3 mm].

5. Conclusions

1. As the PSA changes within the range of $[-12$ mm, 0 mm], there is a noticeable alteration in the fluctuation range of the acceleration signals at the midpoint of the FFSP.
2. As the PSA changes from -12 mm to 0 mm, the concentration of energy distribution in the frequency domain increases. In addition, the fundamental frequency signal of the screen plate does not always equal to the frequency of the external excitation signal at different PSA.

3. By obtaining the nonlinear stiffness coefficients of the screen plate under different PSA, we have concluded that the nonlinear spring-tri-body model can be approximated as the mechanical model of the screen plate under the experimental conditions.
4. As the PSA changes from -12 mm to 0 mm, the motion state of the midpoint of the screen plate transitions from quasi-periodic state to approaching chaotic motion state, and then returns to quasi-periodic motion.
5. The screening efficiency and the misplaced content of oversized particles are only related to amplitude of the vertical acceleration upward along the screen plate, and are independent of the motion state of the screen plate and the amplitude of the vertical acceleration downward along the screen plate. In this study, the optimum range of PSA is $[-9$ mm, -3 mm].

Author Contributions: Conceptualization, Y.W., W.Y. and D.L.; methodology, Y.W. and D.L.; software, R.G.; validation, W.Y. and Z.W.; formal analysis, Y.W.; investigation, W.Y. and D.L.; resources, X.W.; data curation, Y.W.; writing—original draft preparation, Y.W.; writing—review and editing, R.G., W.Y. and D.L.; visualization, Y.W.; supervision, W.Y. and Z.W.; project administration, X.W.; funding acquisition, X.W. All authors have read and agreed to the published version of the manuscript.

Funding: This work was financially supported by the Anhui Province Major Science and Technology Achievements Engineering Research and Development Special Project under Grant (No. 202103c08020007) and the Fundamental Research Funds for the Central Universities (No. 2022YJSHH15).

Data Availability Statement: The data presented in this study are available on request from the corresponding author due to the external policy.

Conflicts of Interest: The authors declare no conflict of interest.

References

1. Guo, X.; Tang, Y.G.; Eble, C.F.; Wang, Y.F.; Li, P.Y. Study on petrographic characteristics of devolatilization char/coke related to coal rank and coal maceral. *Int. J. Coal Geol.* **2020**, *227*, 103504. [[CrossRef](#)]
2. Asif, M.; Bak, C.U.; Saleem, M.W.; Kim, W.S. Performance evaluation of integrated gasification combined cycle (IGCC) utilizing a blended solution of ammonia and 2-amino-2-methyl-1-propanol (AMP) for CO₂ capture. *Fuel* **2015**, *160*, 513–524. [[CrossRef](#)]
3. Bhattacharya, M.; Rafiq, S.; Bhattacharya, S. The role of technology on the dynamics of coal consumption–economic growth: New evidence from China. *Appl. Energ.* **2015**, *154*, 686–695. [[CrossRef](#)]
4. Wang, W.F.; Qin, Y.; Wang, J.Y.; Li, J.A. Partitioning of Hazardous Trace Elements during Coal preparation. *Procedia Earth Planet. Sci.* **2009**, *1*, 838–844.
5. Zhang, B.; Luo, Z.F.; Zhao, Y.M.; Lv, B.; Song, S.L.; Duan, C.L.; Chen, Z.Q. Effect of a high-density coarse-particle layer on the stability of a gas–solid fluidized bed for dry coal beneficiation. *Int. J. Miner. Process.* **2014**, *132*, 8–14. [[CrossRef](#)]
6. Blaschke, W.; Nycz, R. Clean coal-preparation barriers in Poland. *Appl. Energy* **2003**, *74*, 343–348. [[CrossRef](#)]
7. Li, D.; Wu, D.S.; Xu, F.G.; Lai, J.H.; Shao, L. Literature overview of Chinese research in the field of better coal utilization. *J. Clean. Prod.* **2018**, *185*, 959–980. [[CrossRef](#)]
8. Singh, G.; Kumar, S.; Sehgal, S.S.; Gill, H.S. Investigation on the impact of physical properties of the coal-ash slurries on the erosion wear performance of WC coated steel by using Image processing technique. *Int. J. Coal Prep. Util.* **2020**, *42*, 2406–2426. [[CrossRef](#)]
9. Peng, L.P.; Jiang, H.S.; Chen, X.H.; Liu, D.Y.; Feng, H.H.; Zhang, L.; Zhao, Y.M.; Liu, C.S. A review on the advanced design techniques and methods of vibrating screen for coal preparation. *Powder Technol.* **2019**, *347*, 136–147. [[CrossRef](#)]
10. Pwc, A.; Mds, A.; Rdm, B. Separation performance of double deck banana screens-Part 1: Flow and separation for different accelerations. *Miner. Eng.* **2009**, *22*, 1218–1229.
11. Jiang, H.; Qiao, J.; Zhou, Z.; Zhao, Y.; Yang, Y.; Duan, C.; Luo, Z.; Cai, L.; Wang, S.; Pan, M. Time evolution of kinematic characteristics of variable-amplitude equal-thickness screen and material distribution during screening process. *Powder Technol.* **2018**, *336*, 350–359. [[CrossRef](#)]
12. Afsari, O.; Hashemnia, K. Optimized design of a linear vibrating screen based on efficiency maximisation and mesh wear minimisation employing discrete element method. *Particuology* **2024**, *90*, 307–322. [[CrossRef](#)]
13. Linhares, T.B.; Vimieiro, C.B.S. Evaluation of the movement performance of a vibrating screen due to machining errors on the shaft. *Eng. Fail. Anal.* **2024**, *161*, 108260. [[CrossRef](#)]
14. Arifuzzaman, S.M.; Dong, K.; Yu, A. Process model of vibrating screen based on DEM and physics-informed machine learning. *Powder Technol.* **2018**, *410*, 117869. [[CrossRef](#)]

15. Ogunmodimu, O.; Govender, I.; Mainza, A.N.; Franzidis, J. Development of a mechanistic model of granular flow on vibrating screens. *Miner. Eng.* **2021**, *163*, 106771. [[CrossRef](#)]
16. Linhares, T.B.; Vimieiro, C.B.S. Analysis of the dynamic forces acting on a vibrating screen and its support structure using a scale model. *Measurement* **2021**, *176*, 109179. [[CrossRef](#)]
17. Makinde, O.A.; Ramatsetse, B.I.; Mpofu, K. Review of vibrating screen development trends: Linking the past and the future in mining machinery industries. *Int. J. Miner. Process.* **2015**, *145*, 17–22. [[CrossRef](#)]
18. Fernandez, J.W.; Cleary, P.W.; Sinnott, M.D.; Morrison, R.D. Using SPH one-way coupled to DEM to model wet industrial banana screens. *Miner. Eng.* **2011**, *24*, 741–753. [[CrossRef](#)]
19. Dong, H.L.; Liu, C.S.; Zhao, Y.M.; Zhao, L.L. Review of the development of dry coal preparation theory and equipment. *Adv. Mater. Res.* **2013**, *619*, 239–243. [[CrossRef](#)]
20. Chen, B.X.; Yu, C.; Gong, S.P.; Wang, X.W. Dynamic characteristics of LIWELL flip-flow screen panel and particle movement. *Chem. Eng. Sci.* **2021**, *245*, 116853. [[CrossRef](#)]
21. Zheng, G.F.; Zhu, J.B.; Xia, W.D.; Wang, P.P.; Liu, S.L. Banana flip-flow screen benefits coal preparation. *Filtr. Separat.* **2016**, *53*, 38–41.
22. Chen, Z.; Huang, L.; Jiang, H.; Zhao, Y.; Liu, C.; Duan, C.; Zhang, B.; Yang, G.; Chai, J.; Ban, H.; et al. Application of screening using a flip-flow screen and shallow groove dense-medium separation in a steam coal preparation plant. *Int. J. Coal Prep. Util.* **2020**, *42*, 2438–2451. [[CrossRef](#)]
23. Guofeng, Z.; Kunwei, P.; Ningning, X. Simulation of particles motion on a double vibrating flip-flow screen surface based on FEM and DEM coupling. *Powder Technol.* **2023**, *412*, 118422.
24. Cao, Y.; Wang, X. Application of flip—Flow screen in raw coal deep screening of Tangjiahui Coal Preparation Plant. *Coal Eng.* **2020**, *52*, 110–113.
25. Geng, R.H.; Yu, C.; Wang, Y.X. Effect of External Moisture Content on Screening Performance of Vibrating Flip-Flow Screen and Circular Vibrating Screen. *Minerals* **2023**, *13*, 585. [[CrossRef](#)]
26. Yu, C.; Lin, D.D.; Xu, N.N. DEM simulation of particle flow and separation in a vibrating flip-flow screen. *Particuology* **2023**, *73*, 113–127. [[CrossRef](#)]
27. Li, H.X.; Liu, C.S.; Shen, L.; Zhao, L.L.; Li, S. Kinematics characteristics of the flip-flow screen with a crankshaft-link structure and screening analysis for moist coal. *Powder Technol.* **2021**, *394*, 326–335. [[CrossRef](#)]
28. Wang, W.A.; Pan, M.; Duan, C.L.; Jiang, H.S.; Zhao, Y.M.; Lu, H.D. Dry deep screening of spodumene and its mineral processing technology. *Miner. Eng.* **2022**, *179*, 107445. [[CrossRef](#)]
29. Wu, B.; Zhang, X.; Niu, L.K.; Xiong, X.Y.; Dong, Z.X.; Tang, J. Research on Sieving Performance of Flip-Flow Screen Using Two-Way Particles-Screen Panels Coupling Strategy. *IEEE Access* **2019**, *7*, 124461–124473. [[CrossRef](#)]
30. Zhao, G.F.; Wang, X.W.; Lin, D.D.; Xu, N.N.; Yu, C.; Geng, R.H. Study of Double-Deck Vibrating Flip-Flow Screen Based on Dynamic Stiffness Characteristics of Shear Springs. *Minerals* **2021**, *11*, 928. [[CrossRef](#)]
31. Xu, N.N.; Yu, C.; Gong, S.P.; Zhao, G.F.; Lin, D.D.; Wang, X.W. Numerical study and multi-objective optimization of flexible screening process of flip-flow screen: A DEM-FEM approach. *Adv. Powder Technol.* **2022**, *33*, 103650. [[CrossRef](#)]
32. Yu, C.; Wang, X.W.; Pang, K.F.; Zhao, G.F.; Sun, W.P. Dynamic Characteristics of a Vibrating Flip-Flow Screen and Analysis for Screening 3 mm Iron Ore. *Shock Vib.* **2020**, *2020*, 1031659. [[CrossRef](#)]
33. Li, H.X.; Liu, C.S.; Shen, L.; Zhao, L.L. Vibration Characteristics of an Industrial-Scale Flip-Flow Screen with Crank-Link Structure and Parameters Optimization. *Shock Vib.* **2021**, *2021*, 2612634. [[CrossRef](#)]
34. Yu, C.; Wang, X.; Gong, S. Stability analysis of the screening process of a vibrating flip-flow screen. *Miner. Eng.* **2021**, *163*, 106794. [[CrossRef](#)]
35. Mu, L. Study on Load-Bearing Characteristics for Rubber Spring at Low Temperature. Master's Thesis, Hunan University of Technology, Zhuzhou, China, 2016.
36. Mokem, F.; Buckjohn, C.; Siewe, M. Nonlinear analysis and analog simulation of a piezoelectric buckled beam with fractional derivative. *Eur. Phys. J. Plus* **2017**, *132*, 344. [[CrossRef](#)]
37. Wang, W.; Xu, H.; Peng, F. Kinematic characteristics of key structures and time evolution law of material distribution characteristics during flip-flow screening. *Miner. Eng.* **2023**, *201*, 108241. [[CrossRef](#)]
38. Huang, J.; Zhou, W.; Zhu, W. Quasi-periodic motions of high-dimensional nonlinear models of a translating beam with a stationary load subsystem under harmonic boundary excitation. *J. Sound Vib.* **2019**, *462*, 114870. [[CrossRef](#)]
39. Zou, M.; Liu, C.; Wu, L.; Wang, Z. Influence of tensional amount on dynamic parameters of unilateral driven flip-flow screen surface. *J. China Coal Soc.* **2018**, *43*, 571–577.
40. Zhao, Y.; Liu, C.; Fan, M. Research on acceleration of elastic flip—flow screen surface. *Inter. J. Miner. Process.* **2000**, *59*, 267–274. [[CrossRef](#)]
41. Xiong, X.; Niu, L.; Gu, C. Vibration characteristics of an inclined flip-flow screen panel in banana flip-flow screens. *J. Sound Vib.* **2017**, *411*, 108–128. [[CrossRef](#)]
42. Wang, W.; Hou, X.; Duan, C. Dynamic model of the flip-flow screen-penetration process and influence mechanism of multiple parameters. *Adv. Powder Technol.* **2022**, *33*, 103814. [[CrossRef](#)]
43. Lin, D.; Xu, N.; Yu, C. Nonlinear model of vibrating flip-flow screens that considers the effects of screen panels. *IEEE Access* **2022**, *10*, 34246–34259. [[CrossRef](#)]

44. Tang, J.; Niu, L.; Xiong, X. Viscoelasticity of rubber springs affects vibration characteristics of a flip-flow screen with the high G value. *IEEE Access* **2020**, *8*, 26950–26965. [[CrossRef](#)]
45. Schulz, N.F. Separation Efficiency, Society of Mining Engineer. *AIME* **1970**, *247*, 81–87.
46. Yu, C.; Pang, K.F.; Geng, R.H. Comparison of flip-flow screen and circular vibrating screen vibratory sieving processes for sticky fine particles. *Miner. Eng.* **2022**, *187*, 107791. [[CrossRef](#)]
47. Santo, D.; Mencik, J.; Goncalves, P. On the multi-mode behavior of vibrating rods attached to nonlinear springs. *Nonlinear Dyn* **2020**, *100*, 2187–2203. [[CrossRef](#)]
48. Ganguly, S.; Roy, K. Performance assessment of time-domain damage indicators based on output-only measurement and Poincaré map: A comparative review on nonlinear structures. *Measurement* **2023**, *216*, 112847. [[CrossRef](#)]
49. Jiang, H.; Zhao, Y.; Duan, C. Properties of technological factors on screening performance of coal in an equal-thickness screen with variable amplitude. *Fuel* **2017**, *188*, 511–521. [[CrossRef](#)]

Disclaimer/Publisher’s Note: The statements, opinions and data contained in all publications are solely those of the individual author(s) and contributor(s) and not of MDPI and/or the editor(s). MDPI and/or the editor(s) disclaim responsibility for any injury to people or property resulting from any ideas, methods, instructions or products referred to in the content.